

Charge order with unusual star-of-David lattice in monolayer NbTe₂

Taiki Taguchi,¹ Katsuaki Sugawara,^{1,2,3,4} Hirofumi Oka,² Tappei Kawakami,¹ Yasuaki Saruta,¹ Takemi Kato,¹ Kosuke Nakayama,^{1,4} Seigo Souma,^{2,3} Takashi Takahashi,^{1,2,3} Tomoteru Fukumura,^{2,3,5} and Takafumi Sato,^{1,2,3,6}

¹*Department of Physics, Graduate School of Science, Tohoku University, Sendai 980-8578, Japan*

²*Advanced Institute for Materials Research (WPI-AIMR), Tohoku University, Sendai 980-8577, Japan*

³*Center for Science and Innovation in Spintronics (CSIS), Tohoku University, Sendai 980-8577, Japan*

⁴*Precursory Research for Embryonic Science and Technology (PRESTO), Japan Science and Technology Agency (JST), Tokyo 102-0076, Japan*

⁵*Department of Chemistry, Graduate School of Science, Tohoku University, Sendai 980-8578, Japan and*

⁶*International Center for Synchrotron Radiation Innovation Smart (SRIS), Tohoku University, Sendai 980-8577, Japan*

(Dated: December 27, 2022)

Interplay between fermiology and electron correlation is crucial for realizing exotic quantum phases. Transition-metal dichalcogenide (TMD) $1T$ -TaS₂ has sparked a tremendous attention owing to its unique Mott-insulating phase coexisting with the charge-density wave (CDW). However, how the fermiology and electron correlation are associated with such properties has yet to be clarified. Here we demonstrate that monolayer $1T$ -NbTe₂ is a new class of two-dimensional TMD which has the star-of-David lattice similarly to bulk TaS₂ and isostructural monolayer NbSe₂, but exhibits a metallic ground state with an unusual lattice periodicity ($\sqrt{19}\times\sqrt{19}$) characterized by the sparsely occupied star-of-David lattice. By using angle-resolved photoemission and scanning-tunneling spectroscopies in combination with first-principles band-structure calculations, we found that the hidden Fermi-surface nesting and associated CDW formation are a primary cause to realize this unique correlated metallic state with no signature of Mott gap. The present result points to a vital role of underlying fermiology to characterize the Mott phase of TMDs.

One of key challenges in materials science is to find outstanding two-dimensional (2D) materials by reducing the dimensionality from bulk (3D) to 2D, as highlighted by the discovery of room temperature quantum Hall effect in graphene¹. Transition-metal dichalcogenides (TMDs) offer a fertile platform to explore exotic 2D materials, since two-dimensionalization of bulk TMDs often creates fundamentally different physical properties such as the Ising superconductivity associated with the space-inversion-symmetry breaking in monolayer $1H$ -NbSe₂ [ref.2] and the quantum spin Hall insulator phase in monolayer $1T'$ -WTe₂ and $1T'$ -WSe₂ [refs.3,4]. When electron correlation is introduced into 2D systems, even more exotic quantum states would emerge, as exemplified by the discovery of superconductivity on the verge of Mott-insulating phase in twisted bilayer (BL) graphene, where the enhanced electron correlation due to the band narrowing by moiré potential plays a key role⁵. A 2D Mott-insulating state that coexists with charge-density wave (CDW) in monolayer $1T$ -NbSe₂ and TaSe₂ has been also discussed to be triggered by the enhanced electron correlation due to the CDW-induced band narrowing⁶⁻⁸.

A central player for such unique CDW-Mott phase is the star-of-David (soD) cluster of transition-metal atoms, where the corner atom is slightly displaced from the original position towards the central atom [inset to Fig. 3(d)]. In this soD cluster, the half-filling condition to realize the Mott-insulating phase is satisfied, because, as exemplified in the case of bulk $1T$ -TaS₂, twelve electrons at the displaced twelve Ta atoms form 6 fully occupied bands and remaining one electron at the central Ta atom forms a half-filled metallic band⁹⁻¹². However, the mechanism of

CDW-Mott phase in TMDs is still far from being well understood⁶⁻¹⁹, owing to the existence of complex energy bands in the CDW phase. It is still unknown how electron correlation, CDW, and Mott phases are inter-related. It is thus highly important to pin down a key ingredient to realize the Mott phase by exploring ultrathin 2D TMDs. In this regard, monolayer $1T$ -NbTe₂ is a promising target because it is isostructural to Mott-insulating monolayer $1T$ -NbSe₂. Bulk NbTe₂ crystallizes in the $1T$ structure at high temperatures. Below 530 K, it undergoes a structural transition to the monoclinic $1T''$ phase with the $3\times 1\times 3$ periodic lattice distortion²⁰⁻²² associated with the CDW triggered by the Fermi-surface (FS) nesting²³. Superconductivity was observed below $T_C = 0.5$ K [ref.24]. Despite such intensive studies of bulk properties, basic properties such as crystal structure and ground-state characteristics of monolayer NbTe₂ remain unexplored. It is also important to clarify the electronic states of isostructural Se- and Te-based TMDs to understand how the difference in the band character between Se and Te manifests itself in the exotic physical properties such as Mott insulating properties and CDW.

In this paper, we report angle-resolved photoemission spectroscopy (ARPES) and scanning tunneling microscopy (STM) studies on the electronic state of monolayer $1T$ -NbTe₂ fabricated on BL graphene. We uncovered the metallic $\sqrt{19}\times\sqrt{19}$ CDW state coexisting with an unusual soD lattice distortion in $1T$ -NbTe₂ in stark contrast to the gapped Mott-insulating nature of monolayer $1T$ -NbSe₂. We discuss implications of the present results to address the origin of unique CDW-Mott phase in 2D TMDs.

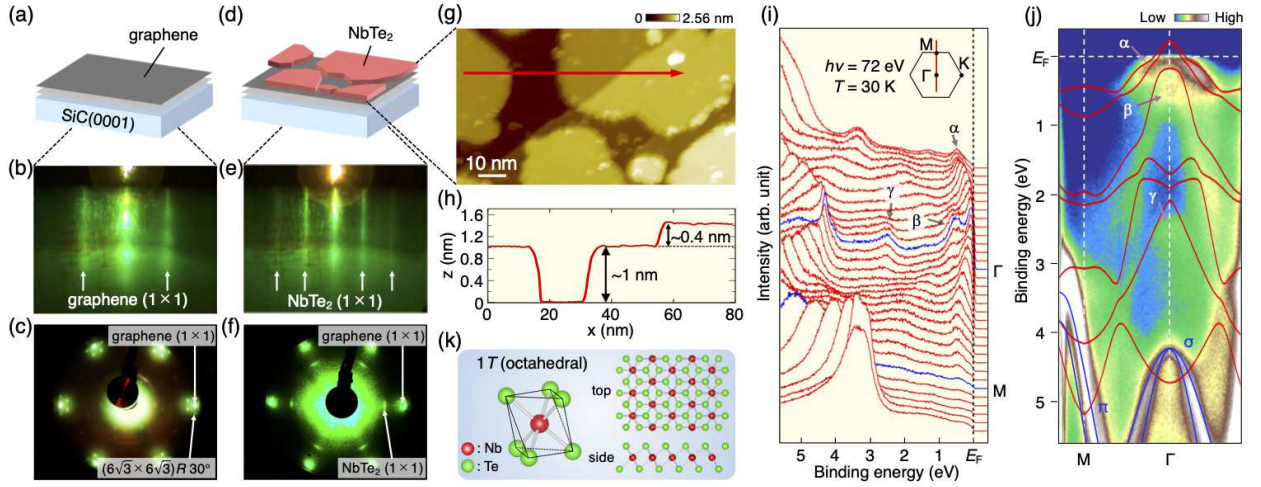


FIG. 1. (a) Schematic view of BL graphene on SiC. (b),(c) RHEED and LEED patterns of bilayer (BL) graphene. (d)-(f) Same as (a) to (c) but for NbTe₂ on BL graphene. (g) Constant-current STM image at $T = 4.8$ K in the surface area of 56×100 nm² (sample bias voltage $V_s = -2$ V, and set-point tunneling current $I_t = 50$ pA). (h) Height profile along a cut indicated by red arrow in (g). (i) EDCs for monolayer NbTe₂ measured at $T = 30$ K with $h\nu = 72$ eV along the ΓM line of NbTe₂ Brillouin zone (inset). (j) Plot of valence-band ARPES intensity for monolayer NbTe₂, compared with the calculated band structure for monolayer 1T-NbTe₂ (red curves) and BL graphene (blue curves). Experimental three holelike bands are labeled as α , β , and γ in (i) and (j). (k) Schematic crystal structure of monolayer 1T-NbTe₂.

Monolayer NbTe₂ films were grown on BL graphene by the molecular-beam-epitaxy (MBE) method. ARPES measurements were carried out using a MBS-A1 electron-energy analyzer (MB Scientific AB) at Tohoku University and a DA-30 electron-energy analyzer (Omicron-Scienta) at beamline BL28 in Photon Factory, KEK. STM measurements were carried out using a custom-made ultrahigh vacuum STM system²⁵. First-principles band-structure calculations were carried out by using the Quantum Espresso code package²⁶ For details, see Appendix A.

First, we present fabrication and characterization of monolayer NbTe₂. To fabricate a NbTe₂ film, we used the van der Waals epitaxy technique by using BL graphene grown on silicon carbide as a substrate [Fig. 1(a)]. Figure 1(b) shows the RHEED (reflection high energy electron diffraction) pattern of BL graphene on 6H-SiC(0001) which signifies a 1×1 streak pattern together with a weaker $6\sqrt{3} \times 6\sqrt{3} R30^\circ$ pattern originating from BL graphene and carbon-mesh layer beneath it, respectively. Corresponding spots are also visible in the LEED (low-energy electron diffraction) pattern in Fig. 1(c). After co-evaporation of Nb and Te atoms onto the substrate kept at 300°C under ultrahigh vacuum, the intensity of $6\sqrt{3} \times 6\sqrt{3}$ spot is reduced and a new 1×1 pattern appears [Figs. 1(d)-(f)]. This behavior is characteristic of TMD ultrathin films, as observed in various monolayer TMDs such as NbSe₂ and TaSe₂ [refs.6-8]. STM measurements revealed the formation of monolayer NbTe₂ islands [Fig. 1(g)] whose height is ~ 1.0 nm [Fig. 1(h)], in rough agreement with the distance between adjacent NbTe₂ layers in bulk 1T-NbTe₂ (~ 0.7 nm)²⁸, supporting

its monolayer nature (note that another 0.4-nm-height step originates from the step of the SiC substrate).

We characterized the overall band structure of monolayer NbTe₂ film by *in-situ* angle-resolved photoemission spectroscopy (ARPES). Figure 1(i) displays the energy distribution curves (EDCs) at $T = 30$ K measured at $h\nu = 72$ eV along the ΓM cut of hexagonal NbTe₂ Brillouin zone. Besides the band structure originating from BL graphene situated at the binding energy (E_B) higher than ~ 3 eV, one can clearly identify several dispersive features originating from NbTe₂ within 3 eV of the Fermi level (E_F). There exist three holelike bands centered at the Γ point; one has a shallow dispersion (labeled as α) within 1 eV of E_F and appears to cross E_F in the vicinity of the Γ point, and the other two have a wider dispersion each topped at $E_B = 0.5$ and 2.5 eV at the Γ point (labeled as β and γ , respectively). To see more clearly the dispersive features, we plot in Fig. 1(j) the ARPES intensity as a function of k_x and E_B , together with the calculated band structure for monolayer 1T-NbTe₂ (red) and BL graphene (blue). One can immediately recognize that the intense features at higher E_B 's well overlap with the calculated π and σ bands of BL graphene. A qualitative matching can be also found for the NbTe₂ bands; the calculated holelike Te 5*p* bands topped at 0.2 eV and 2.1 eV seem to have experimental counterparts although there exist quantitative differences in their energy positions. The calculated holelike bands crossing E_F which are attributed to the Nb 4*d* (outer) and Te 5*p* (inner) orbitals also have a good correspondence with the experimental band which crosses E_F around the Γ point. Such an overall agreement between the experiment and calcu-

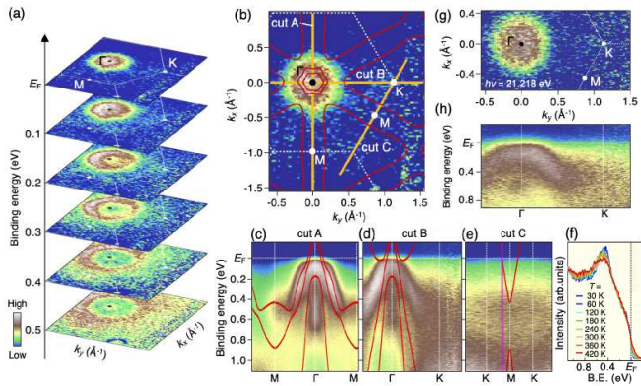


FIG. 2. (a) ARPES-intensity plots as a function of 2D wave vectors (k_x and k_y) for representative E_B slices measured at $T = 30$ K with $h\nu = 72$ eV. (b) Same as (a) but at $E_B = E_F$, overlaid with the calculated Fermi surface (red curves). (c)-(e) ARPES intensity plots near E_F for monolayer NbTe₂ measured along the ΓM (cut A), ΓK (cut B), and KMK (cut C) cuts shown in (b), respectively. Red curves correspond to the calculated band structure for monolayer 1T-NbTe₂. (f) Temperature dependence of EDC measured with $h\nu = 21.218$ eV at the k_F point of the calculated triangular pocket along the MK cut shown by a purple line in (e). (g), (h) Fermi-surface mapping and ARPES-intensity plot as a function of k_y and E_B , respectively, measured with $h\nu = 21.218$ eV at $T = 440$ K for monolayer 1T-NbTe₂.

lation suggests that monolayer NbTe₂ on BL graphene takes the 1T structure [Fig. 1(k)], as corroborated by our STM observation of soD clusters (Fig. 3) which are known to be stabilized only in the 1T structure. It is also inferred from a reasonable matching in the energy position of bands around the Γ point between experiments and calculations shown in Fig. 1(j) that our film is almost stoichiometric (note that a slight disagreement at around the Γ point in higher E_B 's may be explained in terms of the band renormalization due to the electron correlation). The 1T nature of our NbTe₂ film is also supported by the fact that the experimental band structure shows a better agreement with the calculated band structure for the 1T phase than that for the 1H phase (for details, see Appendix B). Also, the E_F -crossing of bands in Figs. 1(i) and 1(j) is distinct from the large Mott gap exceeding 0.2 eV in isostructural monolayer 1T-NbSe₂ and 1T-TaSe₂⁶⁻⁸. We will come back to this point later.

Although the experimental band structure around the Γ point shows a reasonable agreement with the calculation for monolayer 1T-NbTe₂, we found a fatal disagreement of the Fermi-surface topology around the K point. The experimental Fermi surface of monolayer 1T-NbTe₂ is characterized by the existence of a hole pocket only at the Γ point. The holelike nature is directly visualized by the equi-energy contour plot at $T = 30$ K in Fig. 2(a) showing a systematic expansion of the inten-

sity pattern on increasing E_B . As shown in Fig. 2(b), while the calculated Fermi surface consists of a large triangular hole pocket centered at the K point besides the hexagonal one at the Γ point, the spectral weight corresponding to this triangular Fermi surface is missing in the ARPES intensity. To further examine this unusual behavior, we compare the ARPES intensity near E_F along several high-symmetry \mathbf{k} cuts (cuts A-C) with the corresponding calculated band structure in Figs. 2(c)-2(e). Although the experimental band structure along the ΓM cut (cut A) shows a reasonable agreement with the calculation, the holelike Te 5p band along the ΓK cut (cut B) shows a much smaller group velocity and no shallow electron bands exist aside from the hole band. Moreover, along the MK cut (cut C), the spectral feature is broad and flat, and one cannot identify a predicted highly dispersive V-shaped band in the experiment. We have confirmed that the flat feature is robust against the variation in photon energy and light polarization. This suggests that it is not an artifact associated with the matrix-element effect of photoelectron intensity, but is an intrinsic nature of monolayer NbTe₂ (for details, see Appendix C). Temperature-dependent ARPES measurements at the k_F point along the MK cut shown in Fig. 2(f) signify a broad peak at $E_B \sim 0.5$ eV which gradually smears out on increasing temperature but still survives at $T = 420$ K. This peak is likely associated with the formation of CDW (for detailed discussion of its origin, see Appendix D). We have confirmed that the K -centered pocket is absent in a wide temperature range, as highlighted by the Fermi-surface mapping [Fig. 2(g)] as well as the ARPES intensity along the ΓK cut [Fig. 2(h)] measured at $T = 440$ K.

To clarify the mechanism behind the disappearance of a large triangular pocket, we have performed high-resolution STM measurements on a NbTe₂ island [Fig. 3(a)]. The STM image at $T = 4.8$ K in Fig. 3(b) signifies individual Te atoms originating from the top layer of monolayer NbTe₂. Noticeably, the atomic image exhibits a strong intensity modulation; a dark region involving at least 7 Te atoms arranges periodically and forms a hexagonal superlattice surrounded by a brighter region with a honeycomb-shaped pattern. The Fourier-transformation image in the inset to Fig. 3(b) signifies $\sqrt{19} \times \sqrt{19} 23.4^\circ$ superspots (green circles) which correspond to the supercell shown by green rhombus in Fig. 3(b). We found in Fig. 3(c) that the $\sqrt{19} \times \sqrt{19} 23.4^\circ$ superlattice vector well connects the parallel segments of calculated triangular pockets at the K point, consistent with the calculated electronic susceptibility (see Appendix E) [note that the crystal geometry allows the existence of two types of crystal domains ($R \pm 23.4^\circ$) which equally satisfy the nesting condition, as detailed in Appendix F]. These suggest the formation of CDW triggered by the Fermi-surface nesting, which is also inferred from the observation of real-space charge reversal across the CDW gap similarly to the case of KV₃Sb₅ in the CDW phase²⁹ (see Appendix G). The CDW may fully gap out the triangular

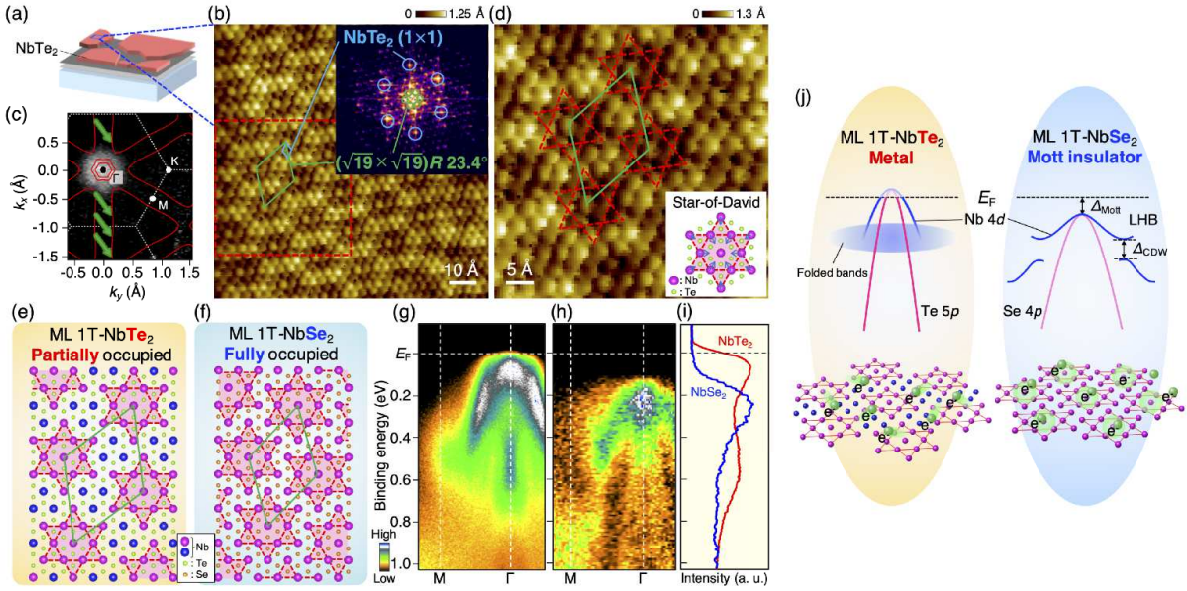


FIG. 3. (a) Schematics of monolayer NbTe₂ islands on BL graphene. (b) STM image in the surface area of $10 \times 10 \text{ nm}^2$ ($V_s = -1.5 \text{ V}$ and $I_t = 0.8 \text{ nA}$). Inset shows Fourier-transform image of (b). (c) Calculated Fermi surface for monolayer 1T-NbTe₂ (red curves), overlaid on the ARPES-intensity plot. The $\sqrt{19} \times \sqrt{19} R 23.4^\circ$ nesting vector is shown by green arrows. (d) STM image magnified in the area shown by red square in (b). V_s and I_t were set to be -1.0 V and 0.8 nA , respectively. Inset shows the illustration of soD cluster. (e),(f) Comparison of the schematic soD lattice between monolayer NbTe₂ and NbSe₂. (g),(h) Near- E_F ARPES intensity along the ΓM cut for monolayer NbTe₂ and NbSe₂, respectively, measured at $T = 30 \text{ K}$. (i) EDC at the Γ point for monolayer NbTe₂ and NbSe₂. (j) Schematics on the relationship between the band dispersion and the soD lattice for monolayer NbTe₂ and NbSe₂.

pocket and create many backfolded subbands. Electron correlation may further smear out the fine structure of each subband, leading to the featureless spectral intensity around the K point as seen in Fig. 2(e). The CDW origin of disappearance of the triangular pocket needs to be experimentally confirmed by modulating the FS-nesting condition by carrier doping, electrical gating, or epitaxial strain. We have estimated the CDW transition temperature (T_{CDW}) to be much above 420 K from the persistence of a peak in the EDC in Fig. 2(f) (note that it was difficult to estimate T_{CDW} from the LEED pattern because superspots were not clearly seen. Such a vague feature of LEED superspots despite the CDW formation was also recognized in some other monolayer TMDs^{30,31}).

To obtain further insights into the characteristics of CDW, we show in Fig. 3(d) a magnified STM image. One may see that the dark region consists of twelve atoms which coincide well with the schematic double triangles rotated by 60° from each other (red broken triangles), a signature of soD cluster (inset) reported in bulk 1T-TaS₂ [refs.11,14,15] as well as monolayer 1T-NbSe₂ and 1T-TaSe₂ [refs.6-8]. These soD clusters form a hexagonal lattice with the $\sqrt{19} \times \sqrt{19} R 23.4^\circ$ periodicity. As a consequence, residual atoms outside the soD clusters are seen as relatively bright spots intervening adjacent soD clusters. It is thus inferred that although isostructural family

of monolayer NbTe₂, NbSe₂, and TaSe₂ (together with bulk 1T-TaS₂) commonly form the soD cluster, that for NbTe₂ partially occupies the lattice [Fig. 3(e); 13 atoms among 19 atoms in the superstructure unit cell are involved in the soD cluster], in stark contrast to the full occupation in other TMDs [Fig. 3(f)]^{6-8,11,14,15}, demonstrating a unique characteristic of monolayer NbTe₂. It is worthwhile to note that, although the $\sqrt{19} \times \sqrt{19} R 23.4^\circ$ periodicity is absent in bulk NbTe₂, it was reported to locally emerge when the bulk sample was pulse heated by electron beam²⁷, and such periodicity was discussed in terms of the CDW driven by the FS nesting²⁸. In this respect, it would be reasonable to infer that the soD modulation observed in monolayer is associated with the formation of CDW, whereas this point needs to be clarified by further experiments.

Now we discuss the relationship between the soD lattice and Mott characteristics. We suggest that the occupation of soD clusters is crucial for understanding the electronic properties at low temperature. Monolayer NbSe₂ is an insulator as seen from the spectral-weight suppression around E_F in the ARPES intensity [Fig. 3(h)] and the apparent energy-gap opening in the EDC at the Γ point [Fig. 3(i)]. This insulating gap was attributed to the Mott-Hubbard gap⁶, because the half-filling condition is satisfied for each soD cluster and there are no other

conducting electrons because of the fully occupied nature of the soD lattice. On the other hand, in NbTe₂, half-filling condition for the Nd 4*d* orbital is globally violated because the Te 5*p* band participates in the Fermi surface. Also, electron hopping between the soD and outside-soD regions could disturb the effective half-filling nature in a single soD cluster and deteriorate the electron localization. These lead to the metallic nature as seen from the sizable spectral weight at E_F in the EDC at the Γ point [see Fig. 3(i)].

The observed intriguing spectral difference between monolayer NbTe₂ and NbSe₂ is also explained in terms of fermiology. As shown in Fig. 3(c), the calculated Fermi surface in the normal state for monolayer NbTe₂ consists of two hole pockets at the Γ point associated with the E_F -crossing of the topmost Nb 4*d* and Te 5*p* bands [schematically shown in Fig. 3(j)], besides a large triangular pocket centered at the K point due to the Nb 4*d* band. On the other hand, these small pockets at the Γ point are absent in the calculation for monolayer NbSe₂ [ref.32] because the Se bands are pulled downward and fully occupied [Fig. 3(j)], as in the case of other chalcogenides^{7,33}. Since the total volume of Fermi surface must be identical between NbTe₂ and NbSe₂ according to the Luttinger theorem, such a difference causes the change in the volume of Nd 4*d* pocket and the resultant modification in the Fermi-surface topology³². This argument is also supported by estimating the carrier number in the observed Fermi surface. The result indicates 1.1 electrons/unit-cell for the Nd-4*d* triangular pocket in NbTe₂ while it is 1.0 electrons/unit-cell for NbSe₂. The deviation from the half-filling condition in NbTe₂ is ascribed to the extra Te 5*p* hole carriers. Such a difference in the fermiology leads to the difference in the Fermi-surface-nesting vector, i.e. $\sqrt{19}\times\sqrt{19}R23.4^\circ$ for NbTe₂ and $\sqrt{13}\times\sqrt{13}R13.9^\circ$ for NbSe₂. Since the small pockets at the Γ point in NbTe₂ are not well connected with each other by the nesting vector, a gapless \mathbf{k} region remains in the CDW phase, contributing to the absence of Mott characteristics of NbTe₂ in contrast to NbSe₂ where the small pocket is intrinsically absent. In this regard, it is very important to systematically fabricate monolayer NbSe_{2-x}Te_x films and investigate the Mott-transition characteristics as a function of x .

One may wonder how the above interpretation based on the real space (occupation of soD) is reconciled with that of the momentum-space (fermiology). The small hole pocket at the Γ point seen by ARPES may be attributed to the outside-soD region observed by STM. However, this argument is too simplistic because the electron localization in the real space is incompatible with the formation of energy band that requires non-local nature in the real space. This in return suggests that the soD and outside-soD regions are not phase separated and electrons can coherently hop between these two regions. This scenario seems consistent with the dI/dV curves in the STM data which smoothly evolve across the boundary of two regions (see Appendix H). In this context, it

is inferred that a small but finite atomic displacement takes place even in the outside-soD region. A sophisticated diffraction study is necessary to clarify this point.

Now we discuss the difference between the metallic NbTe₂ and Mott-insulating NbSe₂ in terms of the effective electron correlation. Since the on-site Coulomb energy U for Nb 4*d* electrons is expected to be similar between NbSe₂ and NbTe₂, a crucial parameter to determine the effective coulomb energy U/W is the bandwidth W in the CDW phase. Since the reconstructed Brillouin zone for NbTe₂ is smaller than that for NbSe₂ due to the larger superlattice unit cell ($\sqrt{19}\times\sqrt{19}$ vs $\sqrt{13}\times\sqrt{13}$), the reconstructed subbands are expected to be flatter in NbTe₂ than in NbSe₂ when one assumes that the strength of CDW potential is similar. This leads to smaller W and resultantly larger U/W in NbTe₂ suggestive of the stronger ‘‘Mottness’’ in NbTe₂. However, this is opposite to our observation, suggesting a less important role of electron correlation to account for the difference between NbTe₂ and NbSe₂. It is noted though that this conjecture is not fully supported by the current experiment because each subband is hard to resolve due to the strong spectral broadening. Another alternative explanation to account for the difference between the metallic NbTe₂ and insulating NbSe₂ is that the Te 5*p* band with wide bandwidth (which is even wider than that of bulk 1*T*-TaS₂ in the nearly commensurate CDW phase¹³) crosses E_F and reduces the effective electron correlation to prevent this system from the Mott transition.

In conclusion, we have performed ARPES and STM combined with first-principles band calculations to study the electronic structure of monolayer 1*T*-NbTe₂ which is characterized by a partially occupied soD lattice possibly associated with the CDW formation. The present observation demonstrates that the formation of soD lattice is not a sufficient condition to realize the Mott-insulating phase which coexists with CDW, while it has been discussed as a necessary condition in bulk 1*T*-TaS₂ and monolayer TMDs. We also found that the underlying Fermi-surface topology and associated hidden Fermi-surface nesting play a crucial role to control the key electronic properties such as periodicity of superlattice, occupation of soD lattice, and Mott-insulating vs metallic properties. The present result opens a pathway toward switching and controlling the Mott-insulating and CDW phases via fermiology engineering in ultrathin TMDs.

ACKNOWLEDGMENTS

We thank Y. Nakata, M. Kitamura, K. Horiba, and H. Kumigashira for their help in the ARPES experiments. This work was supported by JST-CREST (no. JPMJCR18T1), JST-PRESTO (no. JPMJPR20A8), Grant-in-Aid for Scientific Research on Innovative Areas ‘‘Topological Materials Science’’ (JSPS KAKENHI Grant numbers JP15H05853, and JP15K21717), Grant-in-Aid for Scientific Research on Innovative Areas ‘‘Discrete Ge-

ometric Analysis for Materials Design” (JSPS KAKENHI Grant numbers 20H04624), Grant-in-Aid for Scientific Research (JSPS KAKENHI Grant numbers JP18H01821, and JP21H01757), Science research projects from Shi-

madzu Science Foundation, and World Premier International Research Center, Advanced Institute for Materials Research. T. Kawakami and T. Kato acknowledges support from GP-Spin at Tohoku University.

- ¹ K. S. Novoselov, A. K. Geim, S. V. Morozov, D. Jiang, M. I. Katsnelson, I. V. Grigorieva, S. V. Dubonos, and A. A. Firsov, *Nature* **87**, 197 (2005).
- ² X. Xi, Z. Wang, W. Zhao, J.-H. Park, K. T. Law, H. Berger, L. Forró, J. Shan, and K. F. Mak, *Nat. Phys.* **12**, 139 (2016).
- ³ S. Tang, C. Zhang, D. Wong, Z. Pedramrazi, H.-Z. Tsai, C. Jia, B. Moritz, M. Claassen, H. Ryu, S. Kahn, J. Jiang, H. Yan, M. Hashimoto, D. Lu, R. G. Moore, C.-C. Hwang, C. Hwang, Z. Hussain, Y. Chen, M. M. Ugeda, Z. Liu, X. Xie, T. P. Devereaux, M. F. Crommie, S.-K. Mo, and Z.-X. Shen, *Nat. Phys.* **13**, 683 (2017).
- ⁴ P. Chen, W. W. Pai, Y.-H. Chan, W.-L. Sun, C.-Z. Xu, D.-S. Lin, M.Y. Chou, A.-V. Fedorov, and T.-C. Chiang, *Nat. Commun.* **9**, 2003 (2018).
- ⁵ Y. Cao, V. Fatemi, S. Fang, K. Watanabe, T. Taniguchi, E. Kaxiras, and P. Jarillo-Herrero, *Nature* **556**, 43 (2018).
- ⁶ Y. Nakata, K. Sugawara, R. Shimizu, Y. Okada, P. Han, T. Hitosugi, K. Ueno, T. Sato, and T. Takahashi, *NPG Asia Mater.* **8**, e321 (2016).
- ⁷ Y. Nakata, T. Yoshizawa, K. Sugawara, Y. Umemoto, T. Takahashi, and T. Sato, *ACS Appl. Nano Mater.* **1**, 1456 (2018).
- ⁸ Y. Chen, W. Ruan, M. Wu, S. Tang, H. Ryu, H.-Z. Tsai, R. Lee, S. Kahn, F. Liou, C. Jia, O. R. Albertini, H. Xiong, T. Jia, Z. Liu, J. A. Sobota, A. Y. Liu, J. E. Moore, Z.-X. Shen, S. G. Louie, S.-K. Mo, and M. F. Crommie, *Nat. Phys.* **16**, 218 (2020).
- ⁹ J. A. Wilson, F. J. DiSalvo, and S. Mahajan, *Adv. Phys.* **24**, 117 (1975).
- ¹⁰ P. Fazekas and E. Tosatti, *Philos. Mag. B* **39**, 229 (1979).
- ¹¹ R. E. Thomson, B. Burk, A. Zettl and J. Clarke, *Phys. Rev. B* **49**, 16899 (1994).
- ¹² P. Fazekas and E. Tosatti, *Physica B & C* **99**, 183 (1980).
- ¹³ R. Ang, Y. Tanaka, E. Ieki, K. Nakayama, T. Sato, L. J. Li, W. J. Lu, Y. P. Sun, and T. Takahashi, *Phys. Rev. Lett.* **109**, 176403 (2012).
- ¹⁴ L. Ma, C. Ye, Y. Yu, X. F. Lu, X. Niu, S. Kim, D. Feng, D. Tománek, Y.-W. Son, X. H. Chen, and Y. Zhang, *Nat. Commun.* **7**, 10956 (2016).
- ¹⁵ D. Cho, G. Gye, J. Lee, S.-H. Lee, L. Wang, S.-W. Cheong, and H. W. Yeom, *Nat. Commun.* **8**, 392 (2017).
- ¹⁶ S.-H. Lee, J. S. Goh, and D. Cho, *Phys. Rev. Lett.* **122**, 106404 (2019).
- ¹⁷ Y. D. Wang, W. L. Yao, Z. M. Xin, T. T. Han, Z. G. Wang, L. Chen, C. Cai, Y. Li, and Y. Zhang, *Nat. Commun.* **11**, 4215 (2020).
- ¹⁸ C. J. Butler, M. Yoshida, T. Hanaguri, and Y. Iwasa, *Nat. Commun.* **11**, 2477 (2020).
- ¹⁹ L. Liu, H. Yang, Y. Huang, X. Song, Q. Zhang, Z. Huang, Y. Hou, Y. Chen, Z. Xu, T. Zhang, X. Wu, J. Sun, Y. Huang, F. Zheng, X. Li, Y. Yao, H.-J. Gao, and Y. Wang, *Nat. Commun.* **12**, 1978 (2021).
- ²⁰ K. Selte and A. Kjekshus. *Acta. Chem. Scand.* **19**, 258 (1965).
- ²¹ J. A. Wilson and A. D. Yoffe, *Adv. Phys.* **18**, 193 (1969).
- ²² B. B. Brown, *Acta. Cryst.* **20**, 264 (1966).
- ²³ C. Battaglia, H. Cercellier, F. Clerc, L. Despont, M. G. Garnier, C. Koitzsch, P. Aebi, H. Berger, L. Forró, and C. Ambrosch-Draxl, *Phys. Rev. B* **72**, 195114 (2005).
- ²⁴ S. Nagata, T. Abe, S. Terashima, Y. Ishihara, and K. Tsusumi, *Phys. B* **194-196**, 1981 (1994).
- ²⁵ K. Iwaya, T. Ohsawa, R. Shimizu, Y. Okada, and T. Hitosugi, *Sci. Technol. Adv. Mater.* **19**, 282 (2018).
- ²⁶ P. Giannozzi, S. Baroni, N. Bonini, M. Calandra, R. Car, C. Cavazzoni, D. Ceresoli, G. L. Chiarotti, M. Cococcioni, I. Dabo, A. D. Corso, S. de Gironcoli, S. Fabris, G. Fratesi, R. Gebauer, U. Gerstmann, C. Gougoussis, A. Kokalj, M. Lazzeri, L. Martin-Samos, N. Marzari, F. Mauri, R. Mazzarello, S. Paolini, A. Pasquarello, L. Paulatto, C. Sbraccia, S. Scandolo, G. Sclauzero, A. P. Seitsonen, A. Smogunov, P. Umari, and R. M. Wentzcovitch, *J. Phys.: Condens. Matter.* **21**, 395502 (2009).
- ²⁷ J. van Landuyt, G. van Tendeloo, and S. Amerinckx *Phys. Stat. Sol* **26**, 585 (1974).
- ²⁸ J. A. Wilson, *Phys. Rev. B* **17**, 3880 (1978).
- ²⁹ Y.-X. Jiang, J.-X. Yin, M. M. Denner, and N. Shumiya, B. R. Ortiz, G. Xu, Z. Guguchia, J. He, M. S. Hossain, X. Liu, J. Ruff, L. Kautzsch, S. S. Zhang, G. Chang, I. Belopolski, Q. Zhang, T. A. Cochran, D. Multer, M. Litskevich, Z.-J. Cheng, X. P. Yang, Z. Wang, R. Thomale, T. Neupert, S. D. Wilson, and M. Z. Hasan, *Nat. Mater.* **20**, 1353 (2021).
- ³⁰ H. Ryu, Yi Chen, H. Kim, H.-Z. Tsai, S. Tang, J. Jiang, F. Liou, S. Kahn, C. Jia, A. A. Omrani, J. H. Shim, Z. Hussain, Z.-X. Shen, K. Kim, B. I. Min, C. Hwang, M. F. Crommie, and S.-K. Mo, *Nano Lett.* **18**, 689 (2018).
- ³¹ P. M. Coelho, K. N. Cong, M. Bonilla, S. Kolekar, M.-H. Phan, J. Avila, M. C. Asensio, I. I. Oleynik, and M. Batzill, *J. Phys. Chem. C* **123**, 14089 (2019).
- ³² A. Kikuchi and S. Tsuneyuki, *Surf. Sci.* **409**, 458 (1998).
- ³³ Y. Umemoto, K. Sugawara, Y. Nakata, T. Takahashi, and T. Sato, *Nano Res.* **12**, 165 (2019).
- ³⁴ T. Kawakami, K. Sugawara, T. Kato, T. Taguchi, S. Souma, T. Takahashi, and T. Sato, *Phys. Rev. B* **104**, 045136 (2021).
- ³⁵ A. Soumyanarayanan, M. M. Yee, J. van Wezel, D. J. Rahn, K. Rossnagel, E. W. Hudson, M. R. Norman, and J. E. Hoffman, *Proc. Natl. Acad. Sci. USA*, **110**, 1623 (2013).
- ³⁶ M. D. Johannes and I. I. Mazin, *Phys. Rev. B* **77**, 165135 (2008).

Appendix A: Sample fabrication, ARPES measurements, and band calculations

High-quality monolayer NbTe₂ films were grown on bilayer (BL) graphene by the molecular-beam epitaxy (MBE) method in an ultrahigh vacuum of 5×10^{-10} Torr. BL graphene was grown by annealing an *n*-type Si-rich

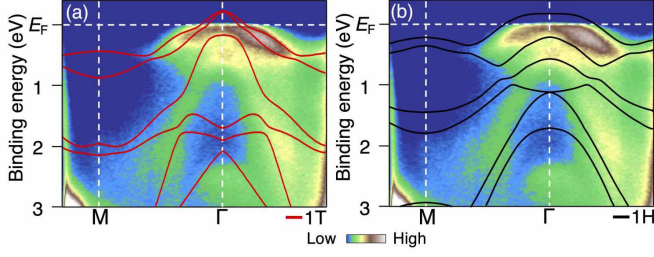


FIG. 4. (a), (b) ARPES intensities of monolayer NbTe₂ compared with the calculated band dispersion for monolayer 1*T*-NbTe₂ (red curves) and monolayer 1*H*-NbTe₂ (black curves), respectively.

6H-SiC(0001) single-crystal wafer^{6,7} by resistive heating at 1100 °C for 30 min in an ultrahigh vacuum better than 1.0×10^{-9} Torr. Monolayer NbTe₂ film was grown by co-evaporating Nb and Te on the BL graphene substrate. The substrate temperature was kept at 300 °C during the epitaxy. The as-grown film was annealed at 300 °C for 30 min to improve the crystallinity, and then transferred to the ARPES-measurement chamber without breaking vacuum. The growth process was monitored in real-time by reflection high-energy electron diffraction (RHEED).

Scanning tunneling microscopy (STM) measurements were carried out using a custom-made ultrahigh vacuum STM system²⁵. Te capping (~ 10 nm thick) for surface protection of NbTe₂ film was removed in the STM chamber by Ar⁺ ion sputtering for 30 min and annealing at 250 °C for 30 min. STM measurements were carried out with an electrochemically etched W tip at 4.8 K under UHV below 2.0×10^{-10} Torr. All STM images were obtained in constant current mode. ARPES measurements were carried out using a MBS-A1 electron-energy analyzer with a high-flux helium discharge lamp at Tohoku University and a DA-30 electron energy analyzer with synchrotron radiation at the beamline BL-28A at Photon Factory (KEK). The He I α resonance line ($h\nu = 21.218$ eV) and linearly polarized light of $h\nu = 72$ eV were used to excite photoelectrons. The energy and angular resolutions were set to be 16-30 meV and 0.2-0.3 °C, respectively. The Fermi level (E_F) of samples was referenced to that of a gold film deposited onto the sample substrate.

First-principles band-structure calculations for free-standing monolayer 1*T*- and 1*H*-NbTe₂ were carried out by using the Quantum-Espresso code²⁶. Spin-orbit interactions were included in the calculation. The plane-wave cutoff energy and the k-point mesh were set to be 70 Ry and $12 \times 12 \times 1$, respectively. Thickness of the inserted vacuum layer for monolayer was set to be ~ 10 Å.

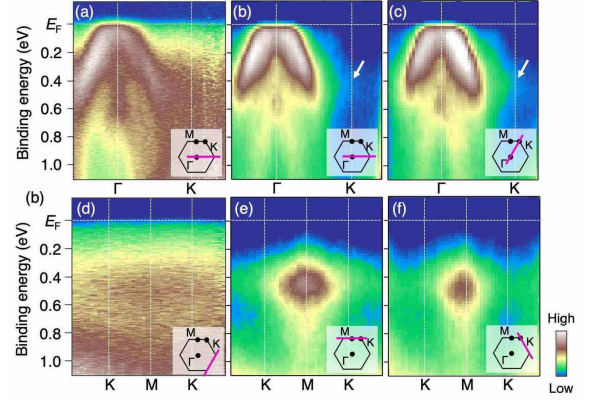


FIG. 5. (a), (b) ARPES intensities along the ΓK cut obtained at $h\nu = 21.218$ eV with linear horizontal light and at $h\nu = 75$ eV with right circular polarized light, respectively. (c) Same as (b) but obtained along another ΓK cut rotated by 60° with respect to the ΓK cut in (b). (d)-(f), Same as (a)-(c) cut, but measured along the MK cut. White arrows in (b) and (c) indicate the location of flat feature.

Appendix B: Comparison between ARPES intensity and band calculations for monolayer 1*T*/1*H*-NbTe₂

To clarify the possibility of different crystal structures, we have carried out band-structure calculations for monolayer NbTe₂ for 1*T* and 1*H* phases. Figures 4(a) and 4(b) show the APRES intensity along the ΓM cut overlaid by the calculated band structure for monolayer 1*T*- and 1*H*-NbTe₂, respectively [note that the calculation does not take into account the formation of star-of-David (soD) lattice]. One can see an overall agreement between experiment and calculation for the 1*T* case, such as a weakly dispersive holelike band at $E_B = E_F - 0.1$ eV and a highly dispersive holelike band at $E_B = 0.3-1.5$ eV, whereas the matching between experiment and calculation is relatively poor for the 1*H* case [Fig. 4(b)]. This supports the 1*T* nature of our NbTe₂ film.

Appendix C: Photon-energy and light-polarization dependences of band structure in monolayer NbTe₂

We performed ARPES measurements along the ΓK and KMK cuts with different sample-light geometry and photon energy ($h\nu$) to clarify the influence from the matrix-element effect of photoelectron intensity to the ARPES intensity. Figures 5(a) and 5(b) show the ARPES intensity along the ΓK cut at $h\nu = 21.218$ eV with linear horizontal polarization and at $h\nu = 75$ eV with right circular polarization, respectively. At $h\nu = 21.218$ eV [Fig. 5(a)], one can recognize a broad non-dispersive feature around the K point at E_B of ~ 0.5 eV, in addition to a highly dispersive holelike band centered at the Γ point. This flat feature is likely associated with the formation of CDW. As shown in Fig. 5(b), a similar

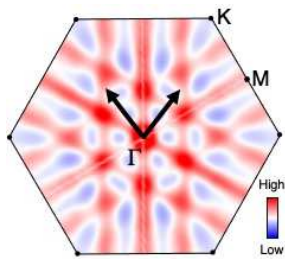


FIG. 6. Intensity plot of the calculated imaginary part of electronic susceptibility $\text{Im}\chi(\mathbf{q})$ for monolayer $1T\text{-NbTe}_2$. Arrows correspond to $\mathbf{q} = 1/\sqrt{19}\mathbf{G}$ nesting vectors.

flat feature is also observed at $h\nu = 75$ eV around the K point (indicated by white arrow), whereas its intensity is largely suppressed. As shown in Fig. 5(c), such a weak and flat feature also exists along another ΓK cut rotated by 60° with respect to the ΓK cut in Fig. 5(b). We find that the flat feature is also recognized along the MK cut with different $h\nu$'s and light polarizations, as shown in Figs. 5(d)-5(f). These results suggest that the existence of observed flat feature (i.e. the absence of a triangular pocket predicted by the DFT calculation) is robust against the variation in photon energy and light polarization. This suggests that the flat feature is not an experimental artifact associated with the matrix-element effect of photoelectron intensity, but is an intrinsic feature of monolayer $1T\text{-NbTe}_2$.

Appendix D: Origin of a flat band around the K point for monolayer NbTe_2

We discuss the origin of a flat feature at $E_B \sim 0.5$ eV around the K point observed in Fig. 2 and Fig. 5. We have considered some possible mechanisms unrelated to the CDW, such as (i) the band gap, (ii) the Anderson gap, and (iii) the Mott-Hubbard gap. The possibility (i) is ruled out because the DFT calculation of monolayer NbTe_2 fails to reproduce the flat band and a finite energy gap. The possibility (ii) is also unlikely because our NbTe_2 film is close to stoichiometry and the ARPES spectrum around the K point (Fig. 2 of the main text) does not show a power-law behavior against E_B expected from the disorder-induced Coulomb gap. The possibility (iii) is also ruled out because the gap size Δ of ~ 0.5 eV is too large compared to the Mott-Hubbard gap of isostructural $1T\text{-NbSe}_2$ ($\Delta \sim 0.1$ eV) despite the expectation of a similar on-site Coulomb energy. Taking into account these points, we think that the flat band is associated with the CDW gap formation.

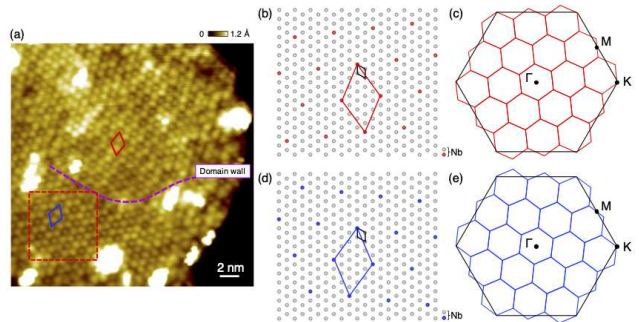


FIG. 7. (a), STM image at $T = 4.8$ K in the surface area of 25×25 nm² on NbTe_2 island ($V_s = -1.6$ V, and $I_t = 0.1$ nA). (b) Real-space configuration of Nb atoms (open circles) and superlattice unit cell (red rhombus) for the $\sqrt{19} \times \sqrt{19}R - 23.4^\circ$ superstructure and (c) corresponding reconstructed Brillouin zone (red) drawn on the original 1×1 Brillouin zone (black). (d), (e) Same as (b) and (c), but for the $R + 23.4^\circ$ superstructure.

Appendix E: Calculated electronic susceptibility for monolayer NbTe_2

To clarify the origin of CDW in monolayer NbTe_2 , we calculated the electronic susceptibility $\chi(\mathbf{q})$ based on the calculated Fermi surface shown in Fig. 2(b). Figure 6 shows the imaginary part of calculated electronic susceptibility [$\text{Im}\chi(\mathbf{q})$] for monolayer $1T\text{-NbTe}_2$. One can recognize three straight lines running along the ΓM direction. Same lines also appear along the other two equivalent ΓM directions rotated by $\pm 60^\circ$ from each other. These lines are mainly associated with the parallel segments of the calculated triangular pockets. One can see that two types of nesting vectors \mathbf{q} for $\sqrt{19} \times \sqrt{19}R + 23.4^\circ$ and $\sqrt{19} \times \sqrt{19}R - 23.4^\circ$ superstructures suggested from the STM data are located near the intersection of straight lines at which the $\text{Im}\chi(\mathbf{q})$ value shows an overall enhancement. This supports the Fermi-surface-instability-driven CDW in monolayer NbTe_2 . It is noted that the electronic susceptibility does not show sharp peak or strong divergence at the corresponding nesting vector. Similar behavior was also recognized in other 2D TMDs, such as $1T\text{-VTe}_2$ and $2H\text{-NbSe}_2$ ^{34–36}.

Appendix F: Two types of crystal domains in monolayer NbTe_2 on bilayer graphene

We found two types of domain structures associated with the $\sqrt{19} \times \sqrt{19}R - 23.4^\circ$ star-of-David (soD) lattice by STM measurements. Figure 7(a) shows the STM image of monolayer $1T\text{-NbTe}_2$ island on bilayer graphene. One can identify existence of two types of superstructures. One has a $\sqrt{19} \times \sqrt{19}R - 23.4^\circ$ periodicity (red rhombus)

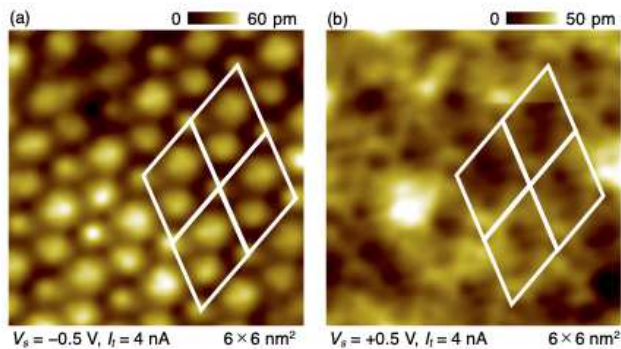


FIG. 8. (a), (b) STM images at $T = 4.8$ K in the surface area of 6×6 nm² measured at (a) negative ($V_s = -0.5$ V, $I_t = 4$ nA) and (b) positive ($V_s = +0.5$ V, $I_t = 4$ nA) bias voltage. White rhombus corresponds to the $\sqrt{19} \times \sqrt{19} R 23.4^\circ$ superstructure unit cell.

and another is rotated by 13.2° with respect to the former one (blue rhombus). The latter domain is assigned to the superstructure with $\sqrt{19} \times \sqrt{19} R + 23.4^\circ$ by taking into account the 6-fold symmetry of NbTe₂ (i.e. $13.2^\circ = 60^\circ - 23.4^\circ - 23.4^\circ$). The existence of two types of domains is naturally expected from the real-space configuration of Nb atoms and the supercell [Figs. 7(b) and 7(d)] as well as the corresponding Brillouin zones [Figs. 7(c) and 7(e)]. At the boundary between the $R + 23.4^\circ$ and $R - 23.4^\circ$ domains, a domain wall is recognized [purple dashed curve of Fig. 7(a)].

Appendix G: STM images across E_F for monolayer NbTe₂

We performed STM measurements at negative and positive bias voltages across the CDW gap for monolayer NbTe₂. As clearly seen in Fig. 8, the high electron-density region characterized by bright-intensity spots at negative bias voltage [Fig. 8(a)] turns into the low electron-density region at positive bias voltage [Fig. 8(b)], similarly to the case of KV₃Sb₅ [ref.8]. This supports the real-space charge reversal and the CDW origin of the observed V-shaped gap for monolayer 1T-NbTe₂.

Appendix H: Local density of states for monolayer NbTe₂

Figure 9(a) shows the STM image at $T = 4.8$ K in the surface area of 6×6 nm² for monolayer NbTe₂. Filled cir-

cles represent the measurement position of dI/dV curves inside the soD cluster (red and black circles) and outside it (blue and green circles). Figure 9(b) shows the dI/dV curves for monolayer NbTe₂ measured at $T = 4.8$ K. The color of curves shows the correspondence to the measurement position in Fig. 9(a). One can recognize several

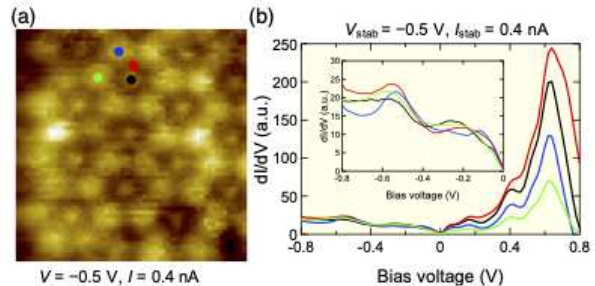


FIG. 9. (a), STM image at $T = 4.8$ K in the surface area of 6×6 nm² for monolayer NbTe₂. (b) dI/dV curves measured at four representative positions inside the soD cluster [red and black filled circles in (a)] and outside it (blue and green ones). Correspondence between the measurement position and dI/dV curve is shown by coloring. Inset shows an expansion in the negative bias-voltage region. dI/dV spectra were recorded with an open feedback loop using a lock-in technique with a modulation voltage of 20 mV at 987 Hz. The setpoints of voltage and current (V_{stab} and I_{stab} , respectively) to stabilize the tip before opening feedback loop are indicated in (b).

peak features in both positive and negative bias voltages irrespective of the location of surface, and there is no abrupt change in the dI/dV curve across the boundary between the inside- and outside-soD regions. Expanded image in the negative-bias voltage region in the inset to Fig. 9(b) signifies broad humps at around -0.2 eV and -0.55 eV, which are associated with the Te 5p bands at the Γ point and the flat band at ~ 0.5 eV around the K point observed by ARPES, respectively [Figs. 2(c) and 2(d)]. One can also see the V-shaped density of states (DOS) at E_F supportive of the absence of an insulating energy gap and appearance of a soft gap, in stark contrast to a large Mott gap in monolayer 1T-NbSe₂ and 1T-TaSe₂ [ref. 6,7,8]. Interestingly, the V-shaped DOS resembles that at the boundary between the metallic and Mott-insulating domains in bulk 1T-TaS₂ [ref.14,15]. The soft-gap nature with residual DOS at E_F seen by STM is also consistent with the ARPES data showing a finite Fermi-edge cut-off associated with the Te 5p band around the Γ point seen in Fig. 2.